


RESEARCH

Open Access

All-fiber device for single-photon detection



Yue Dai^{1†}, Kunpeng Jia^{1*†}, Guanghao Zhu¹, Hui Li¹, Yue Fei¹, Yuqing Guo¹, Hang Yuan¹, Hao Wang¹, Xiaoqing Jia^{1,2}, Qingyuan Zhao¹, Lin Kang^{1,2}, Jian Chen¹, Shi-ning Zhu¹, Peiheng Wu^{1,2}, Zhenda Xie^{1*} and Labao Zhang^{1,2*} 

[†]Yue Dai and Kunpeng Jia contributed equally to this work.

*Correspondence: jiakunpeng@nju.edu.cn; xiezhenda@nju.edu.cn; Lzhang@nju.edu.cn

¹ School of Electronic Science and Engineering, National Laboratory of Solid State Microstructures, Key Laboratory of Intelligent Optical Sensing and Manipulation, School of Physics, College of Engineering and Applied Sciences, and Collaborative Innovation Center of Advanced Microstructures, Nanjing University, Nanjing 210093, P. R. China

² Hefei National Laboratory, Hefei 230088, China

Abstract

Fiber components form the standard not only in modern telecommunication but also for future quantum information technology. For high-performance single-photon detection, superconducting nanowire single-photon detectors (SPDs) are typically fabricated on a silicon chip and fiber-coupled for easy handling and usage. The fiber-to-chip interface hinders the SPD from being an all-fiber device for full utilization of its excellent performance. Here, we report a scheme of SPD that is directly fabricated on the fiber tip. A bury-and-planar fabrication technique is developed to improve the roughness of the substrate for all-fiber detectors' performance for single-photon detection with amorphous molybdenum silicide (MoSi) nanowires. The low material selectivity and universal planar process enable fabrication and packaging on a large scale. Such a detector responds to a broad wavelength range from 405 nm to 1550 nm at a dark count rate of 100 cps. The relaxation time of the response pulse is ~ 15 ns, which is comparable to that of on-chip SPDs. Therefore, this device is free from fiber-to-chip coupling and easy packaging for all-fiber quantum information systems.

Keywords: Fiber, Single-photon detection, Bury-and-planar, Coupling-free

Introduction

Similar to the conduction cable in the electrical system, the optical fiber links the components in the optical system, whether in the classical or quantum regime [1–5]. Traditionally, optical fibers are used to transmit photons, such as flying qubits, to transmit quantum information over long distances [6] between discrete devices with ultralow loss. Recent advances indicate that optical fibers can also be used as a substrate material to be directly integrated with a variety of advanced micro/nano optical devices, taking full advantage of plug-and-play operations and coupling-free features, which is known as lab-on-fiber technology [7–10]. The lab-on-fiber framework hosts ultracompact labs, which can disruptively enlarge the conventional fiber-optics functionalities. By sophisticated fabrication on fiber tips, devices including optical cavities [11, 12], metalenses [13] and nanoelectromechanical systems [14] are realized with all-fiber geometry, enabling broad applications such as sensing and imaging [9, 13, 15–20]. Efforts have also been made for fiber-based photon detection [14, 21], while the detector for a single photon

remains challenging, which governs the qubit rate, fidelity, and error rate of the whole system for quantum information technology.

With superior performances of a low dark count rate, low timing jitter (~ 3 ps) [22], and high detection efficiency ($\sim 99.5\%$ @1350 nm) [23], chip-based superconducting nanowire single-photon detectors (SPDs) provide a powerful tool for quantum information technology [24]. For a few applications, such as random number generation, local photon detection can be performed on the same chip as photon state generation and processing [25, 26]. However, in most applications, such as quantum information processing [27, 28], quantum key distribution [29, 30], and optical quantum computing [31, 32], the SPD is more important as a stand-alone unit and must be fiber-coupled for easy plug-and-play operations. As a result, the fiber-to-chip interface cannot be avoided and will inhibit the high performance of SPD in terms of efficiency, stability and integration.

Traditional on-chip SPDs are fabricated by a planar process in a vertical [23, 33] (Fig. 1(a)) or horizontal [34–36] (Fig. 1(b)) coupling architecture. The optical interface between the optical fiber and SPDs is formed by either free-space optical component assemblies [36] or an optical waveguide (e.g., grating [34, 37] and taper waveguide [38]). For the scheme of commercial solutions, free-space coupling is aided by a zirconia sleeve coupling detector. Simple assembly of key-shape detectors into a zirconia sleeve has become a widely used solution but suffers from extra heat load and risk of misalignment and thus extra loss in a cryostat [36]. For an optical waveguide scheme [34, 36, 39, 40] (see Fig. 1(b)), a nanowire on top of the waveguide absorbs photons through the evanescent field. This scheme accomplishes an absorption efficiency near unity by adjusting the length of the nanowire, while challenges lie in achieving mode matching with coupling

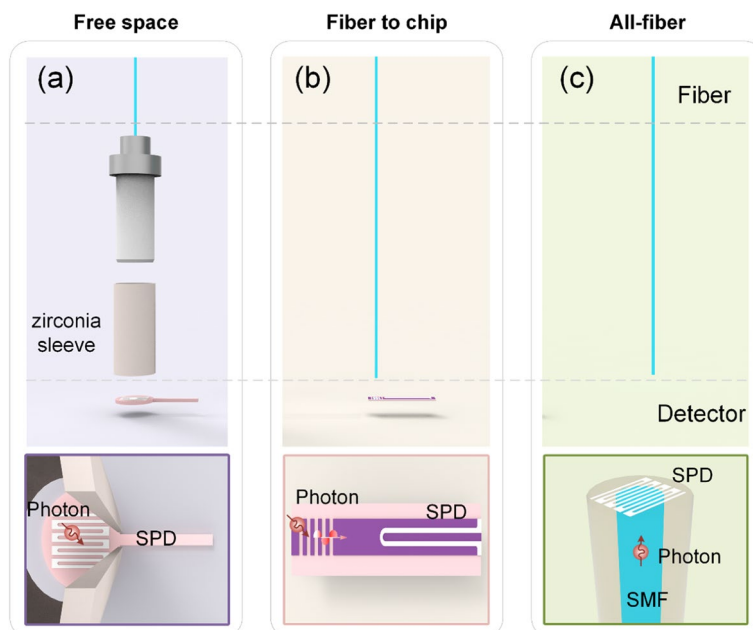


Fig. 1 **a** Schematic of conventional free space coupling. Lower panel: key-shaped substrate with SPD [23, 33]. **b** Schematic of the conventional grating coupling from the fiber to the on-chip waveguide. Lower panel: rectangular silicon substrate with SPD [34, 35]. **c** Schematic of the single-mode fiber-based direct coupling. Lower panel: fiber-based SPD

elements on the optical interfaces, and extra attenuation may be induced by fabrication errors even if sophisticated design and complex fabrication flow have been applied. Therefore, it is a straightforward solution that SPD is directly integrated into optical fibers to take advantage of the convenience brought by optical fibers as an optical-field standard, such as plug-and-play operation, neglectable attenuation, massive scalability, etc. However, the small size and flexibility of optical fibers make direct planar technology a challenge in all-fiber devices.

Here, we demonstrate a fiber-based superconducting nanowire single-photon detector (FSPD) (see Fig. 1(c)) by a bury-and-planar process. Such geometry completely avoids the fiber-to-chip interface, and the advantages are twofold. First, the direct optical coupling on the fiber increases the photon utilization fully, considering the negligible propagation loss in a single mode fiber (SMF). Higher integration of the whole system brings upgrades in terms of stabilization and reliability. Second, our structure features an ultralow thermal load due to the extremely low thermal conductivity of the fiber. The sample holder can be smaller than traditional chip-based SNSPDs, which produce less heat leakage of the components connecting room temperature components and the cold head of cryocoolers and is beneficial for cryogenic cooling to the millikelvin level. Benefiting from the broadband spectrum transmission capability of optical fibers, FSPD can be utilized for single-photon detection over a broad spectral range from 405 nm to 1550 nm.

Method

Figure 2(a) is a schematic diagram of our FSPD comprising an on-chip fiber, an SPD, and an external fiber. The SPD is precisely patterned on the fiber core with a misalignment of less than 100 nm. Thus, the additional loss introduced by fabrication error is negligible and much less than it is on-chip or on-waveguides [33, 34, 41, 42]. Here, the system detection efficiency (SDE) of our FSPD architecture includes absorptance A , coupling efficiency η_c from fiber to SPD, and quantum efficiency η_q . For the SPD field, coupling efficiency is usually defined as the efficiency with which incident photons are coupled to the active region of the detector. We are designing the active area ($15\ \mu\text{m} \times 15\ \mu\text{m}$), which is larger than the area of the fiber core. Since the active region completely covers the fiber core, η_c can be regarded as nearly 100%. The quantum efficiency depends on the quality of the nanowire and represents the probability of response when the nanowire absorbs incident photons. According to our previous work [43, 44], a saturation quantum efficiency ($\eta_q \approx 100\%$ at 1550 nm) was achieved. As a result, the system detection efficiency of SPD is dominated by nanowire absorptance A , which can be improved by optimizing the width of nanowire, filling factor, optical cavity and the incident angle of photons for a certain wavelength in the future applications. In this proof-of-concept demonstration, a high A of 41.1% is achieved for our design in the simulation. Finally, the maximum SDE can be estimated as $A \cdot \eta_c \cdot \eta_q \approx 41.1\%$. Note that this value can be improved to as high as 95.9% by further structure optimization, as discussed later in this paper.

Optical fiber can be easily tailored, spliced and stretched in its longitudinal direction; however, the operation on its cross section is technically difficult to achieve due to the submillimeter size. To be compatible with conventional wafer processing technology, we

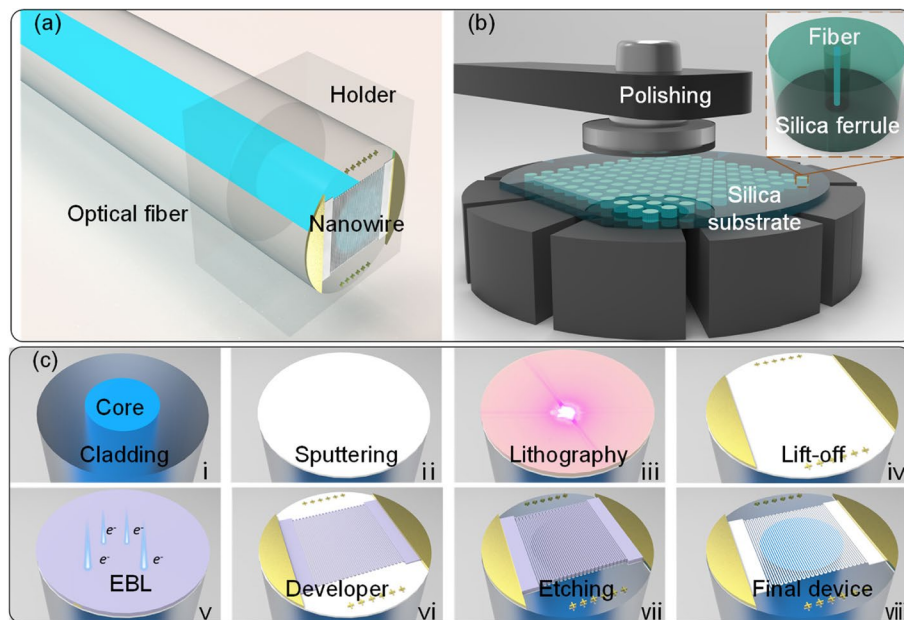


Fig. 2 **a** Schematic of the designed all-fiber device, which consists of an external fiber, an on-chip fiber with a holder, and an SNSPD. **b** Mechanical polishing for very-large-scale on-chip fibers. Inset: An on-chip fiber. In the experiment, we use nine on-chip fibers on the quartz holder. **c** Schematic of the fabrication process of the all-fiber device. i, Cleaning up the on-chip fiber. ii, Magnetron sputtering of the film. iii, Spin-coating the photoresist and lithography. iv, Lift-off Au maker. v, Spin-coating and using EBL. vi, Developer. vii, Reactive ion etching for pattern transfer. viii, Removal of excess PMMA

developed a new bury-and-planar technology for FSPD fabrication. A section of SMF is first mounted in standard glass silica with a diameter of 1.8 mm and then buried and fixed in a silica wafer using epoxy glue. Figure 2(b) shows a schematic of this on-chip fiber geometry with hundreds of fibers, which is suitable for very large-scale fabrication. Smooth substrate surfaces avoid nanowire deformation or splitting and thus performance degradation. We developed the mechanical polishing technique on the fiber tip by burying the single-mode fiber into the homogeneous substrate. By using a sequence of coarse polishing and fine polishing and precisely controlling the polishing speed, we successfully reduce the surface roughness down to 0.5 nm, which is one of the key requirements for high-quality superconducting nanowire growth. Note that the silica ferrule and silica substrate are utilized for the convenience of easy handling and processing, which can be removed later. A meander FSPD is fabricated on an SMF tip, as shown in Fig. 2(c).

A meander FSPD is fabricated on a single-mode fiber tip, as shown in Fig. 2(c). i to Fig. 2(c). vii. Usually, the tip of an on-chip fiber is too dirty to sputter films after direct mechanical polishing. Thus, on-chip fibers should be cleaned in acetone and anhydrous ethanol in ultrasonic environments. A MoSi layer (typically 8 nm thick) is uniformly grown via dc sputtering on the on-chip fiber. MoSi nanowires are easily oxidized in air. As a protective layer for MoSi, the Nb_5N_6 film is deposited on top of the MoSi film via dc magnetron sputtering in situ. The total sheet resistance of the two layers is $214\ \Omega$ per square, and the critical temperature is 5.20 K. The contact pads are defined by lithography and lift-off. The ultraviolet photoresist is spin-coated to a

thickness of approximately $1\ \mu\text{m}$ for exposure of 7 s at $12\ \mu\text{W}/\text{cm}^2$, and the exposed photoresist is developed for 18 s in ZJX-100. After exposure, the sample is prebaked at a heating stage temperature of 90°C for 2 mins. Ti (10 nm) and Au (80 nm) films are sputtered, and lift-off is performed with ultrasound in absolute acetone and ethanol, respectively. Then, electron-resistant PMMA is spun onto the sample and prebaked with PMMA at 180°C for 4 mins. PMMA is most commonly used as a high-resolution positive resist for electron beam lithography (EBL). Approximately 200 nm-thick PMMA is exposed in a 100 kV EBL tool to fabricate nanowires. The nanowire field is designed to be $15 \times 15\ \mu\text{m}^2$ to accomplish near-unity coupled efficiency. The sample is developed in MIBK for 90 s and in isopropyl alcohol for 60 s. The polymethyl methacrylate nanopattern is transferred into MoSi via RIE. The RIE recipe is 76 s CF_4 at 50 W. The sample is soaked in N-methyl pyrrolidone in an 80°C water bath for 30 minutes.

In the EBL process, the insulation substrate results in dramatic backscattering after the incidence of high-energy electrons. Redundant backscattered electrons may lead to overexposure of the electron beam resist. Therefore, we use conductive adhesives and thinner substrates to direct backscattered electrons to the ground to ensure fabrication success. The introduced Nb_5N_6 film in situ not only protected the superconductor films but also guaranteed the resolution ratio of EBL. In e-beam lithography, the resolution is always degenerated due to charge aggregation in this nonconductive substrate. Our Nb_5N_6 film acts as a conductive layer at room temperature, which reduces backscattered electrons, guarantees the resolution of EBL, and avoids a short circuit in superconductor nanowires as a traditional conductive layer.

The lattice mismatch coefficient between the superconducting film and substrate determines the quality of the SPD, which can be calculated as

$$\Delta = \frac{|a_e - a_s|}{a_s}, \quad (1)$$

where a_e and a_s are the lattice constants of the superconducting films and substrates, respectively. However, the fiber material is amorphous without lattice constants, which differs greatly from the widely used polycrystalline superconducting film. Thus, amorphous materials with transition metals, such as molybdenum silicide (MoSi), have become preferred choices for our FSPD realization [45–47]. According to Bardeen–Cooper–Schrieffer theory, the energy gap ($2\Delta_0$) of MoSi can be calculated as [48].

$$2\Delta_0 = 3.53k_B T_c = 2.28\text{meV}, \quad (2)$$

where k_B and T_c are the Boltzmann constant and critical temperature, respectively. This value is lower than that of niobium nitride (NbN) ($2\Delta_0 = 4.90\text{meV}$), which means that the MoSi-based FSPD can produce more quasiparticles under the same incident light conditions and thus features a higher detection efficiency, according to the hot-spot model [49]. Moreover, in our experiment, it is found that $\text{Mo}_x\text{Si}_{1-x}$ ($0 < x < 1$) maintains similar superconducting properties in terms of critical temperature on fiber and silicon substrates, which may also result from its disordered structure. This makes the $\text{Mo}_x\text{Si}_{1-x}$ film easier to apply in other platforms. We used a $\text{Mo}_{0.8}\text{Si}_{0.2}$ alloy target to sputter the superconducting film in an argon (Ar) atmosphere with a fixed deposition speed of

0.9 nm/s. The thickness of the $\text{Mo}_{0.8}\text{Si}_{0.2}$ film is designed to be 8 nm as a result of the trade-off between absorption and quantum efficiency.

Results and discussion

To prevent the ultrathin $\text{Mo}_{0.8}\text{Si}_{0.2}$ film from oxidation and alkalinity in the subsequent process, a 7 nm-thick Nb_5N_6 film as a protective layer is subsequently grown on the $\text{Mo}_{0.8}\text{Si}_{0.2}$ film in situ, which is an insulator [50] and thus will not affect the superconducting properties of the $\text{Mo}_{0.8}\text{Si}_{0.2}$ film at low temperature. Figure 3(a) reveals that the $\text{Mo}_{0.8}\text{Si}_{0.2}$ film has no large crystalline domain. We measured the critical temperature (T_c) of the films at which a normal state transforms into a superconducting state in a liquid helium dewar. The T_c of 8 nm-thick $\text{Mo}_{0.8}\text{Si}_{0.2}$ on the fiber is 5.20 K, which is close to that of $\text{Mo}_{0.8}\text{Si}_{0.2}$ grown on a thermally oxidized silicon wafer [44]. It is worth noting that our scheme involves EBL only once. It greatly simplifies the process complexity and avoids overlay errors compared to chip-based SPD architectures, which require two times. For general free-space SPD architectures [51, 52], deep silicon etching is required for shaping the substrate into a keyhole shape for easy mounting in the ceramic sleeve. Our FSPD is free from fiber-to-chip coupling and easy packaging for all-fiber quantum information systems.

We designed nanowires with a 100 nm width and 200 nm pitch. After reactive ion etching, the average width of the nanowires measured by scanning electron

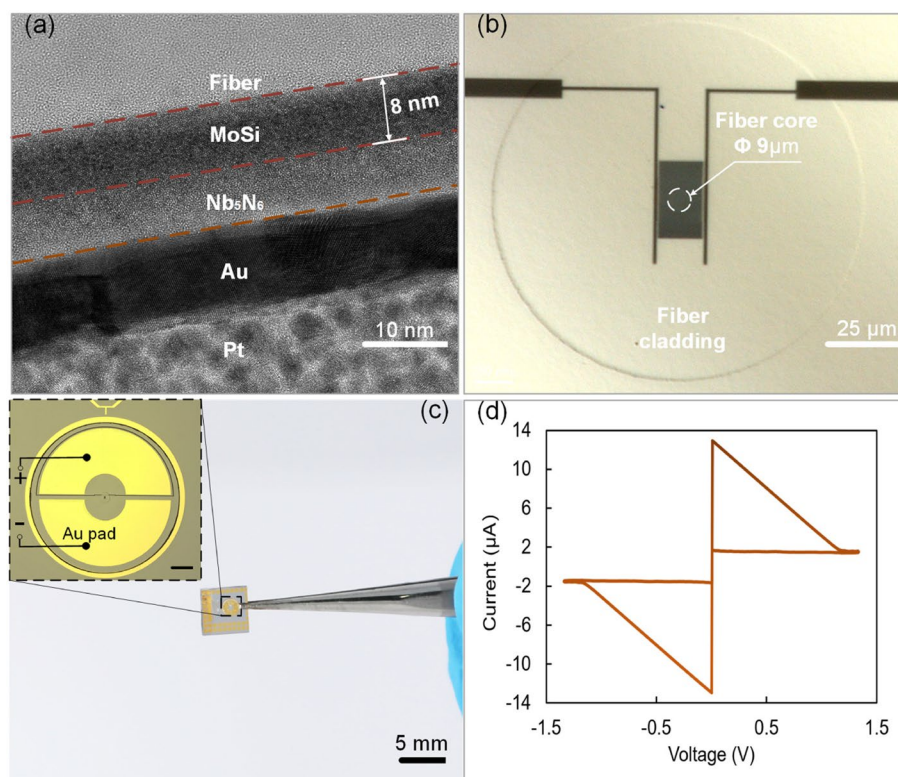


Fig. 3 **a** TEM of the MoSi film and Nb_5N_6 film on the fiber tip. **b** Optical microscope image of the core on the fiber. **c** Photograph of an FSPD. Inset: optical microscope image of FSPD. Scale bar: 250 μm . **d** IV trace curve of the FSPD

microscopy was 78.4 nm. Figure 3(b) is a microscope photograph of the SMF tip with nanowires. With the assistance of the alignment markers, the position of nanowires can be precisely controlled to completely cover the fiber core area, resulting in the highest coupling efficiency from fiber to nanowires. Then, golden pads are connected with readout circuits via aluminum wirebonds, as shown in Fig. 3(c).

We evaluate the FSPD in terms of switching current, electric output pulse, dark count rate, and photon count rate using the experimental setup shown in Fig. 4(a). The experiment was performed with FSPD at a temperature of 45 mK in a dilution refrigerator (Oxford Triton). As shown in Fig. 4(a), a constant voltage source is used to deliver a bias current to the nanowires.

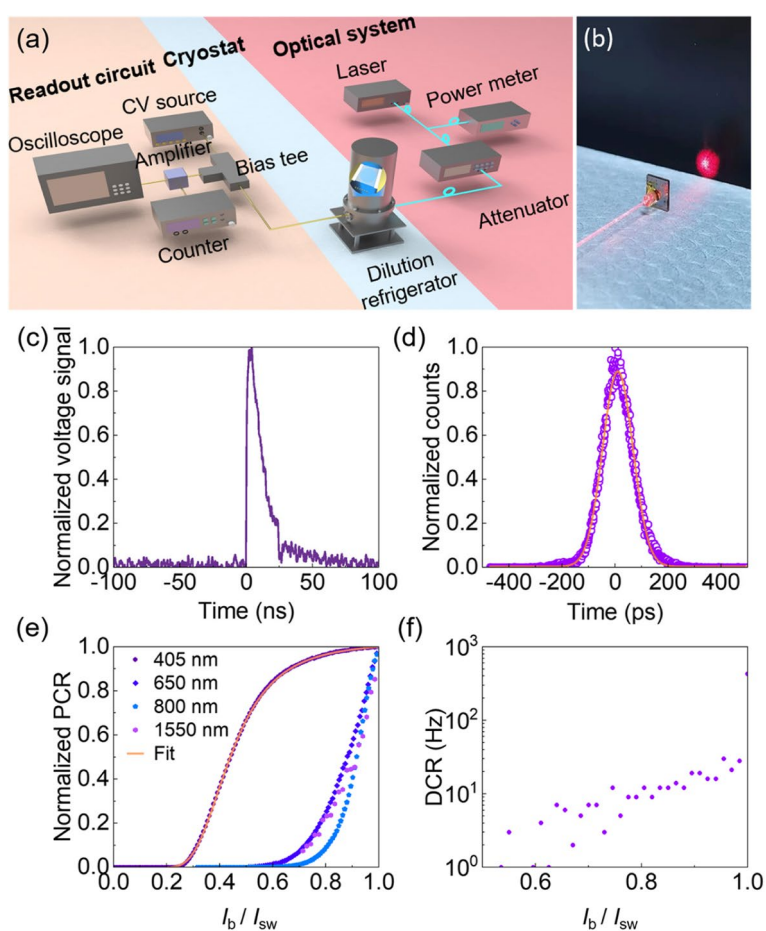


Fig. 4 **a** Experimental setup. For the optical system, the light is divided into two channels. The light in one arm is measured by the power meter (Thorlabs-PM100D), and the light in another arm is attenuated (EXFO FVA-3150) and illuminates the SPD through the fiber. The FSPD only includes fibers and nanowires. The blue lines represent fibers. For the readout circuit, the device is current biased with a voltage source (Keithley 2400 SourceMeter), while the RF port of the bias tee (ZFBT-6GW-FT+, Mini Circuit Inc.) is connected with a low-noise amplifier (MITEQAM-1309). The oscilloscope (KEYSIGHT infiniiVision DSOX6004A) shows the amplified voltage signal. This port is also chosen to connect with the counter (SR400 Gated Photon Counter) for SPD measurement. **b** Photograph of an FSPD transporting red-light source. **c** Oscilloscope persistence map of the electric output pulse at $0.9 I_{sw}$. **d** Histograms of the time-correlated photon counts measured at 405 nm. **e** Normalized photon count rate versus bias current ranging from 405 nm to 1550 nm. **f** Dark count rates versus bias current measured at 45 mK

According to the current tuning curve plotted in Fig. 3(d), after the bias current exceeds the switching current (I_{sw}) of the nanowires, the nanowires enter a normal state. As the bias current decreases, the current of the nanowires is equal to the hysteresis current (I_h), and the nanowires return to the superconducting state. The I_{sw} and I_h of FSPD are measured to be 13.2 μ A and 1.8 μ A, respectively.

Finally, an external fiber is aligned and attached to the FSPD for further characterization, as shown in the photograph in Fig. 4(b). A pulsed laser at 1550 nm wavelength is attenuated to the single photon level and sent to FSPD. As captured by the oscilloscope and shown in Fig. 4(c), FSPD generates response pulses after the nanowires absorb the incident photons, which reflects the current in the nanowires over time. One of the key performances of SPD is the relaxation time (τ), which is the time it takes for SPD to recover from the normal state to the superconducting state and has a large influence on the counting rate as well as the signal-to-noise ratio in quantum optics applications. The relaxation time of SPD is mainly determined by the kinetic inductance, which prevents nanowires from returning to the superconducting state from the normal state. Even with a large area of nanowires ($15 \times 15 \mu\text{m}^2$) and thus high kinetic inductance, our FSPD features a relatively short relaxation time of 15 ns, as shown in Fig. 4(c), compared with the free-space-coupled SPD with the same area of a single MoSi nanowire [47, 53, 54]. While the length of the FSPD is larger than the typical nanowire length used in the optical waveguide scheme, we can meet the requirement for high coupling efficiency and lower recovery time by designing multipixel detectors on the same tip of the fiber. Thus, FSPD with a high-speed response has the potential to take full advantage of the ultrahigh bandwidth.

Time jitter describes the fluctuation of the time arrival moment of the detector pulse obtained using instrumental measurements when the arrival moment of the incident photon is determined. Here, the timing jitter of FSPD is measured to be 114 ps with a 405 nm pulsed laser (pulse width = 51 ps) by a high-speed oscilloscope, as shown in Fig. 4(d). Nanowires with narrower (e.g., 60 nm) widths and cryogenic amplifiers reduce the time jitter of the detector.

Although the FSPD is placed in a dilution refrigerator with low blackbody radiation, its pigtail is at room temperature. As a result, photons from blackbody radiation can travel through the fiber and finally arrive at nanowires. To evaluate the photon count rates of the detector at different wavelengths, we first shielded the stray light at room temperature and measured the dark count rate (DCR). The DCRs for increasing bias current are < 100 cps at $0.9 I_{sw}$, as shown in Fig. 4(f). Then, to test the broadband responsivity of FSPD, we measured the photon count rates (PCRs) with four pulsed lasers at 405 nm, 650 nm, 800 nm and 1550 nm, as shown in Fig. 4(e). As expected, the FSPD responds to all four wavelengths. We normalized the photon counter rate (PCR) to the corresponding highest PCR at different wavelengths, and the quantum efficiency can be derived by fitting the curves. In particular, at a wavelength of 405 nm, the PCR data as a function of normalized bias current are fitted by a sigmoidal curve, and the saturation plateau indicates a quantum efficiency as high as 100%. The quantum efficiency for other bands can be optimized with narrower nanowires and lower gap-energy materials in the future [43, 55]. As a proof-of-concept demonstration, our work focuses on the design of an all-fiber SNSPD and its broadband responsivity by characterizing the quantum efficiency over a wide spectrum.

In this proof-of-concept demonstration, the method of inserting an optical fiber into substrates is designed to meet the standard of planar processes. In contrast to self-assembly [7] and spin-coating [56], higher yields and process reproducibility are possible with such a bury-and-planar method. To further simplify the architecture and improve compatibility, the fiber with SPD on the tip can be released from the holder and spliced with the commercial fiber system. Moreover, nanowire absorptance is now the main limitation on the efficiency of our device according to the aforementioned analysis. Here, we simulate the nanowire absorptance with different incident angles (θ) of the photon from the fiber as the schematic and results shown in Fig. 5(a) and (b), respectively. The numerical computations are performed by COMSOL Multiphysics. We designed meander MoSi nanowires with 80-nm width and 200-nm pitch. The absorptance with Nb₅N₆ is close to the absorptance without Nb₅N₆ in the simulation (Supplementary Information). We only consider the later layer in the simulation. The refractive index of MoSi is 5.4198+4.587i at a wavelength of 1550 nm. Floquet periodicity is used in the Comsol 2D model, and we are only concerned with the cell setup as [57]. When total reflection occurs, refracted light will propagate along the interface, resulting in a greater probability of interaction between nanowires and photons, which is beneficial for photon absorption of nanowires. We optimized the angle of the fiber to achieve total reflection on the fiber tip for greater absorptance of MoSi. Even without a cavity, a near-unity absorption efficiency at 1550 nm can still be obtained (see inset of Fig. 5(b)) when the photon is incident at an angle of total reflection as

$$\theta = \arcsin \frac{n_2}{n_1} = 43.61^\circ, \tag{3}$$

where $n_1=1.4499$ and $n_2=1.0000$ are the refractive index of the core and the air at 1550 nm, respectively. Meander nanowires are sensitive to light polarization. The highest absorption efficiency is obtained when the beam polarization is aligned to the length

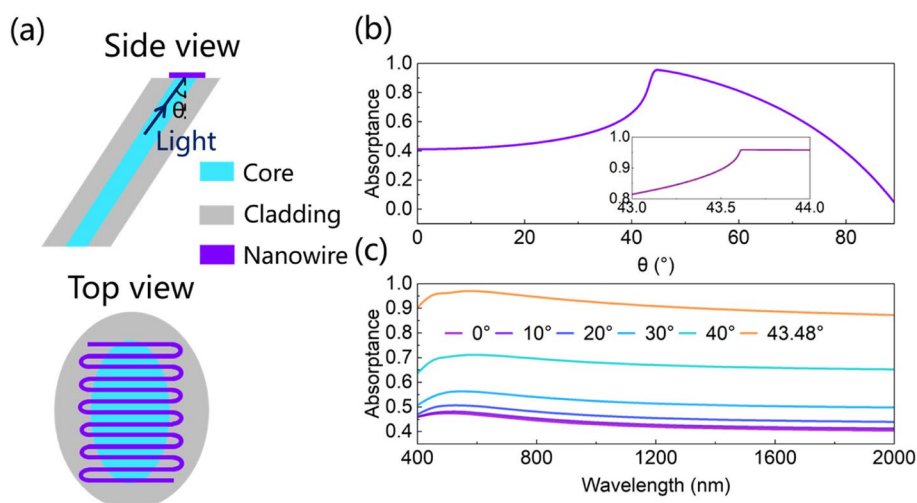


Fig. 5 **a** Schematic of FSPD with incident photons at angle θ . **b** At 1550 nm wavelength, absorbance as a function of the incident angle θ from 0° to 89°. Inset: magnified view with incident angles ranging from 43° to 44°. **c** Simulated absorbance of nanowires as a function of the incident photon wavelength with θ at 0°, 10°, 20°, 30°, 40°, and 43.48°

direction of the nanowires, which can be tuned by the stress-induced birefringence effect in SMF. Thus, we expect that a maximum $SDE = A \cdot \eta_c \cdot \eta_q \approx 95.9\%$ can be achieved with precise control of the fiber cutting angle and proper design of nanowires at 1550 nm, as shown in the inset of Fig. 5(b). More importantly, such a geometry is able to take full advantage of the broadband responsivity of our all-fiber device. As shown in Fig. 5(c), compared with the case of vertical polishing ($\theta = 0^\circ$), the absorptance of nanowires increases with the cutting angle θ and more than doubles over a wide spectrum from 400 nm to 2000 nm with $\theta = 43.48^\circ$. Higher absorptance at a specific wavelength can also be optimized by nesting the nanowire in an optical cavity [58, 59].

Conclusions

In conclusion, we demonstrate a fiber-based superconducting nanowire single-photon detector, which may become an important picture puzzle for future quantum fiber networks. Superconducting nanowires are successfully fabricated on the tip of an SMF through a bury-and-planar process. High-precision micro/nano fabrication ensures perfect alignment between the nanowire and the fiber core; as a result, such architecture enables plug-and-play operation with all fiber optic systems. Our FSPD shows near-unity quantum efficiency at 405 nm and responds to a wide range of wavelengths from the visible to telecom band. This FSPD features a short relaxation time of 15 ns for high-speed communications technology, which can be further reduced by designing shorter nanowires or using a cryogenic temperature amplifier.

Very large-scale quantum photonic circuits are plagued by connection loss and transmission loss. For large-scale quantum photonic circuits requiring light from an external laser, all-fiber devices are a favorable competitor due to their low expense and ease of stable fabrication. In addition, for the need for high-bandwidth information transmission in quantum computing, a high-bandwidth SMF integrated with functional blocks provides a fresh choice [60]. Furthermore, we envisage quantum photonic circuits based on all-fiber devices for a unique mechanism as “quantum photonic circuits on fiber”.

Abbreviations

| | |
|------|---|
| AFM | Atomic force microscopy |
| DCR | Dark count rate |
| EBL | Electron beam lithography |
| FSPD | Fiber-based superconducting nanowire single-photon detector |
| PCR | Photon count rate |
| PSD | Phase sensitive demodulator |
| RF | Radio frequency |
| SDE | System detection efficiency |
| SMF | Single mode fiber |
| SPD | Superconducting nanowire single-photon detector |
| TEM | Transmission electron microscope |

Supplementary Information

The online version contains supplementary material available at <https://doi.org/10.1186/s43074-023-00085-5>.

Additional file 1: Fig. S1. Comparison between FSPD with Nb_3N_6 and FSPD without Nb_3N_6 .

Acknowledgments

The authors thank the technical support from the Collaborative Innovation Center of Advanced Microstructures.

Authors' contributions

L.Z. and Z.X. conceived the concept. Y.D., K.J., L.Z. and Z.X. conceived and optimized the bury-and-planar process. Y.D. and K.J. designed and fabricated the device. Y. D., G. Z., H. L., Y. F. and Y.G. characterized the fabricated devices. Y. D. and H. Y. developed the code for the simulations. Y.D., K.J., L.Z. and Z.X. wrote the manuscript with contributions from all authors. H.W., X.J., Z.Q., L.K. and J.C. provided support for the design of the planar process. S.Z. and P.W. supervised the project. The author(s) read and approved the final manuscript.

Funding

This work is supported by the Innovation Program for Quantum Science and Technology (No. 2021ZD0303401), the National Key R&D Program of China (2019YFA0705000, 2022YFA120018800), the National Natural Science Foundation of China (12033002, 62071218, 62071214, 61801206, 12161141009, 12074175, 51890861, 62293520, 62293523), Key-Area Research and Development Program of Guangdong Province (2020B0303020001), Leading-edge Technology Program of Jiangsu Natural Science Foundation (BK20192001), Zhangjiang Laboratory (ZJSP21A001), the Fundamental Research Funds for the Central Universities, the Priority Academic Program Development of Jiangsu Higher Education Institutions (PAPD), the Recruitment Program for Young Professionals, the Qing Lan Project and the Jiangsu Provincial Key Laboratory of Advanced Manipulating Technique of Electromagnetic Waves, Postgraduate Research & Practice Innovation Program of Jiangsu Province (KYCX22_0141), Jiangsu Planned Projects for Postdoctoral Research Funds (2021K259B).

Availability of data and materials

The datasets used and/or analyzed during the current study are available from the corresponding author on reasonable request.

Declarations

Competing interests

The authors declare that they have no competing interests.

Received: 9 September 2022 Revised: 29 January 2023 Accepted: 1 February 2023

Published online: 07 February 2023

References

1. Arrazola JM, Bergholm V, Brádler K, Bromley TR, Collins MJ, Dhand I, et al. Quantum circuits with many photons on a programmable nanophotonic chip. *Nature*. 2021;591(7848):54–60.
2. Bhaskar MK, Riedinger R, Machielse B, Levonian DS, Nguyen CT, Knall EN, et al. Experimental demonstration of memory-enhanced quantum communication. *Nature*. 2020;580(7801):60–4.
3. Elshaari AW, Pernice W, Srinivasan K, Benson O, Zwiller V. Hybrid integrated quantum photonic circuits. *Nat Photonics*. 2020;14(5):285–98.
4. Qiang X, Zhou X, Wang J, Wilkes CM, Loke T, O'Gara S, et al. Large-scale silicon quantum photonics implementing arbitrary two-qubit processing. *Nat Photonics*. 2018;12(9):534–9.
5. Zhang M, Wang C, Hu Y, Shams-Ansari A, Ren T, Fan S, et al. Electronically programmable photonic molecule. *Nat Photonics*. 2019;13(1):36–40.
6. Cozzolino D, Bacco D, Da Lio B, Ingerslev K, Ding Y, Dalgaard K, et al. Orbital angular momentum states enabling fiber-based high-dimensional quantum communication. *Phys Rev Appl*. 2019;11(6):064058.
7. Galeotti F, Pisco M, Cusano A. Self-assembly on optical fibers: a powerful nanofabrication tool for next generation "lab-on-fiber" optrodes. *Nanoscale*. 2018;10(48):22673–700.
8. Vaiano P, Carotenuto B, Pisco M, Ricciardi A, Quero G, Consales M, et al. Lab on fiber technology for biological sensing applications. *Laser Photonics Rev*. 2016;10(6):922–61.
9. Xiong Y, Xu F. Multifunctional integration on optical fiber tips: challenges and opportunities. *Advanced Photonics*. 2020;2(6):064001.
10. Yang X, Gong C, Zhang C, Wang Y, Yan GF, Wei L, et al. Fiber Optofluidic microlasers: structures, characteristics, and applications. *Laser Photonics Rev*. 2022;16(1):2100171.
11. Giaquinto M, Aliberti A, Micco A, Gambino F, Ruvo M, Ricciardi A, et al. Cavity-enhanced lab-on-fiber technology: toward advanced biosensors and nano-opto-mechanical active devices. *ACS Photonics*. 2019;6(12):3271–80.
12. Ricciardi A, Zimmer M, Witz N, Micco A, Piccirillo F, Giaquinto M, et al. Integrated optoelectronic devices using lab-on-Fiber technology. *Adv Mater Technol*. 2022;7(9):2101681.
13. Consales M, Quero G, Spaziani S, Principe M, Micco A, Galdi V, et al. Metasurface-enhanced lab-on-fiber biosensors. *Laser Photonics Rev*. 2020;14(12):2000180.
14. Chen JH, Liang ZH, Yuan LR, Li C, Chen MR, Xia YD, et al. Towards an all-in fiber photodetector by directly bonding few-layer molybdenum disulfide to a fiber facet. *Nanoscale*. 2017;9(10):3424–8.
15. Plidschun M, Ren H, Kim J, Förster R, Maier SA, Schmidt MA. Ultrahigh numerical aperture meta-fibre for flexible optical trapping. *Light Sci Appl*. 2021;10(1):57.
16. Principe M, Consales M, Micco A, Crescitelli A, Castaldi G, Esposito E, et al. Optical fiber meta-tips. *Light Sci Appl*. 2017;6(3):e16226.
17. Umakoshi T, Saito Y, Verma P. Highly efficient plasmonic tip design for plasmon nanofocusing in near-field optical microscopy. *Nanoscale*. 2016;8(10):5634–40.
18. Zou M, Liao C, Liu S, Xiong C, Zhao C, Zhao J, et al. Fiber-tip polymer clamped-beam probe for high-sensitivity nanoforce measurements. *Light Sci Appl*. 2021;10(1):171.

19. Zhang L, Zhang H, Tang N, Chen X, Liu F, Sun X, et al. 'Plug-and-play' plasmonic metafibers for ultrafast fibre lasers. *Light. Adv. Manuf.* 2022;3:45.
20. Savinov V, Zheludev NI. High-quality metamaterial dispersive grating on the facet of an optical fiber. *Appl Phys Lett.* 2017;111(9):091106.
21. Bayindir M, Sorin F, Abouraddy AF, Viens J, Hart SD, Joannopoulos JD, et al. Metal–insulator–semiconductor optoelectronic fibres. *Nature.* 2004;431(7010):826–9.
22. Korzh B, Zhao Q-Y, Allmaras JP, Frasca S, Autry TM, Bersin EA, et al. Demonstration of sub-3 ps temporal resolution with a superconducting nanowire single-photon detector. *Nat Photonics.* 2020;14(4):250–5.
23. Chang J, Los JWN, Tenorio-Pearl JO, Noordzij N, Gourgues R, Guardiani A, et al. Detecting telecom single photons with 99.5–2.07+0.5% system detection efficiency and high time resolution. *APL Photonics.* 2021;6(3):036114.
24. Gol'tsman GN, Okunev O, Chulkova G, Lipatov A, Semenov A, Smirnov K, et al. Picosecond superconducting single-photon optical detector. *Appl Phys Lett.* 2001;79(6):705–7.
25. Ma X, Yuan X, Cao Z, Qi B, Zhang Z. Quantum random number generation. *npj Quantum. Information.* 2016;2(1):16021.
26. Ren M, Wu E, Liang Y, Jian Y, Wu G, Zeng H. Quantum random-number generator based on a photon-number-resolving detector. *Phys Rev A.* 2011;83(2):023820.
27. Schuck C, Guo X, Fan L, Ma X, Poot M, Tang HX. Quantum interference in heterogeneous superconducting-photonic circuits on a silicon chip. *Nat Commun.* 2016;7(1):10352.
28. Yu Y, Ma F, Luo X-Y, Jing B, Sun P-F, Fang R-Z, et al. Entanglement of two quantum memories via fibres over dozens of kilometres. *Nature.* 2020;578(7794):240–5.
29. Takesue H, Dyer SD, Stevens MJ, Verma V, Mirin RP, Nam SW. Quantum teleportation over 100 km of fiber using highly efficient superconducting nanowire single-photon detectors. *Optica.* 2015;2(10):832.
30. Tang Y-L, Yin H-L, Chen S-J, Liu Y, Zhang W-J, Jiang X, et al. Measurement-device-independent quantum key distribution over 200 km. *Phys Rev Lett.* 2014;113(19):190501.
31. Wang H, Qin J, Ding X, Chen M-C, Chen S, You X, et al. Boson sampling with 20 input photons and a 60-mode interferometer in a 1014 -dimensional hilbert space. *Phys Rev Lett.* 2019;123(25):250503.
32. Zhong H-S, Wang H, Deng Y-H, Chen M-C, Peng L-C, Luo Y-H, et al. Quantum computational advantage using photons. *Science.* 2020;370(6523):1460–3.
33. Marsili F, Verma VB, Stern JA, Harrington S, Lita AE, Gerrits T, et al. Detecting single infrared photons with 93% system efficiency. *Nat Photonics.* 2013;7(3):210–4.
34. Gaggero A, Martini F, Mattioli F, Chiarello F, Cernansky R, Politi A, et al. Amplitude-multiplexed readout of single photon detectors based on superconducting nanowires. *Optica.* 2019;6(6):823.
35. Pernice WHP, Schuck C, Minaeva O, Li M, Goltsman GN, Sergienko AV, et al. High-speed and high-efficiency travelling wave single-photon detectors embedded in nanophotonic circuits. *Nat Commun.* 2012;3(1):1325.
36. Najafi F, Mower J, Harris NC, Bellei F, Dane A, Lee C, et al. On-chip detection of non-classical light by scalable integration of single-photon detectors. *Nat Commun.* 2015;6(1):5873.
37. Buckley SM, Tait AN, Chiles J, McCaughan AN, Khan S, Mirin RP, et al. Integrated-photonic characterization of single-photon detectors for use in neuromorphic synapses. *Phys Rev Appl.* 2020;14(5):054008.
38. Shibata H, Hiraki T, Tsuchizawa T, Yamada K, Tokura Y, Matsuo S. A waveguide-integrated superconducting nanowire single-photon detector with a spot-size converter on a Si photonics platform. *Supercond Sci Tech.* 2019;32(3):034001.
39. Kahl O, Ferrari S, Rath P, Vetter A, Nebel C, Pernice WHP. High efficiency on-chip single-photon detection for diamond nanophotonic circuits. *J Lightwave Technol.* 2016;34(2):249–55.
40. Reithmaier G, Kaniber M, Flassig F, Lichtmanecker S, Müller K, Andrejew A, et al. On-chip generation, routing, and detection of resonance fluorescence. *Nano Lett.* 2015;15(8):5208–13.
41. Li J, Kirkwood RA, Baker LJ, Bosworth D, Erotokritou K, Banerjee A, et al. Nano-optical single-photon response mapping of waveguide integrated molybdenum silicide (MoSi) superconducting nanowires. *Opt Express.* 2016;24(13):13931.
42. Tanner MG, Alvarez LSE, Jiang W, Warburton RJ, Barber ZH, Hadfield RH. A superconducting nanowire single photon detector on lithium niobate. *Nanotechnology.* 2012;23(50):505201.
43. Chen Q, Ge R, Zhang LB, Li FY, Zhang B, Jin FF, et al. Mid-infrared single photon detector with superconductor Mo_{0.8}Si_{0.2} nanowire. *Sci Bull.* 2021;66(10):965–8.
44. Li FY, Han H, Chen Q, Zhang B, Bao H, Dai Y, et al. Saturation efficiency for detecting 1550 nm photons with a 2 x 2 array of Mo_{0.8}Si_{0.2} nanowires at 2.2 K. *Photonics Res.* 2021;9(3):389–94.
45. Charaev I, Morimoto Y, Dane A, Agarwal A, Colangelo M, Berggren KK. Large-area microwire MoSi single-photon detectors at 1550 nm wavelength. *Appl Phys Lett.* 2020;116(24):242603.
46. Caloz M, Perrenoud M, Autebert C, Korzh B, Weiss M, Schönenberger C, et al. High-detection efficiency and low-timing jitter with amorphous superconducting nanowire single-photon detectors. *Appl Phys Lett.* 2018;112(6):061103.
47. Reddy DV, Nerem RR, Nam SW, Mirin RP, Verma VB. Superconducting nanowire single-photon detectors with 98% system detection efficiency at 1550 nm. *Optica.* 2020;7(12):1649–53.
48. Lita AE, Verma VB, Horansky RD, Shainline JM, Mirin RP, Nam S. Materials development for high efficiency superconducting nanowire single-photon detectors. *MRS Online Proc Library.* 2015;1807(1):1–6.
49. Zotova AN, Vodolazov DY. Intrinsic detection efficiency of superconducting nanowire single photon detector in the modified hot spot model. *Supercond Sci Tech.* 2014;27(12):125001.
50. Jia XQ, Kang L, Gu M, Yang XZ, Chen C, Tu XC, et al. Fabrication of a strain-induced high performance NbN ultrathin film by a Nb₅N₆ buffer layer on Si substrate. *Supercond Sci Tech.* 2014;27(3):035010.
51. Gourgues R, Los JWN, Zichi J, Chang J, Kalhor N, Bulgarini G, et al. Superconducting nanowire single photon detectors operating at temperature from 4 to 7 K. *Opt Express.* 2019;27(17):24601–9.
52. Miller AJ, Lita AE, Calkins B, Vayshenker I, Gruber SM, Nam SW. Compact cryogenic self-aligning fiber-to-detector coupling with losses below one percent. *Opt Express.* 2011;19(10):9102–10.

53. Verma VB, Korzh B, Bussieres F, Horansky RD, Dyer SD, Lita AE, et al. High-efficiency superconducting nanowire single-photon detectors fabricated from MoSi thin-films. *Opt Express*. 2015;23(26):33792–801.
54. Wollman EE, Verma VB, Beyer AD, Briggs RM, Korzh B, Allmaras JP, et al. UV superconducting nanowire single-photon detectors with high efficiency, low noise, and 4 K operating temperature. *Opt Express*. 2017;25(22):26792–801.
55. Korneeva YP, Manova NN, Florya IN, Mikhailov MY, Dobrovolskiy OV, Korneev AA, et al. Different single-photon response of wide and narrow superconducting. *Phys Rev Appl*. 2020;13(2):024011.
56. Sun XW, Qiu CY, Wu JY, Zhou HY, Pan T, Mao JM, et al. Broadband photodetection in a microfibergraphene device. *Opt Express*. 2015;23(19):25209–16.
57. Anant V, Kerman AJ, Dauler EA, Yang JKW, Rosfjord KM, Berggren KK. Optical properties of superconducting nanowire single-photon detectors. *Opt Express*. 2008;16(14):10750–61.
58. Baek B, Stern JA, Nam SW. Superconducting nanowire single-photon detector in an optical cavity for front-side illumination. *Appl Phys Lett*. 2009;95(19):191110.
59. Miki S, Takeda M, Fujiwara M, Sasaki M, Wang Z. Compactly packaged superconducting nanowire single-photon detector with an optical cavity for multichannel system. *Opt Express*. 2009;17(26):23557–64.
60. Lecocq F, Quinlan F, Cicak K, Aumentado J, Diddams SA, Teufel JD. Control and readout of a superconducting qubit using a photonic link. *Nature*. 2021;591(7851):575–9.

Publisher's Note

Springer Nature remains neutral with regard to jurisdictional claims in published maps and institutional affiliations.

Submit your manuscript to a SpringerOpen[®] journal and benefit from:

- ▶ Convenient online submission
- ▶ Rigorous peer review
- ▶ Open access: articles freely available online
- ▶ High visibility within the field
- ▶ Retaining the copyright to your article

Submit your next manuscript at ▶ [springeropen.com](https://www.springeropen.com)
